The Flux-Rope Scaling of the Acceleration of Coronal Mass Ejections and Eruptive Prominences

J. Chen[1], C. Marqué[2†], A. Vourlidas[4], J. Krall[1], and P. W. Schuck[1]
[1] *Plasma Physics Division, Naval Research Laboratory, Washington, DC 20375*
[2] *Universities Space Research Association, Naval Research Laboratory, Washington, DC 20375*
[3] *E. O. Hulburt Center for Space Research, Naval Research Laboratory, Washington, DC 20375*
James.Chen@nrl.navy.mil

ABSTRACT

The new flux-rope scaling law of the acceleration of coronal mass ejections (CMEs) derived by Chen and Krall (2003) (Paper 1) is quantitatively tested by comparing the theoretical prediction with the near-Sun acceleration profiles of 13 eruptive prominences (EPs) and four CMEs. A CME and associated EP are assumed to be organized by an underlying magnetic flux rope (MFR) with specific structural and geometrical relationships. The scaling law states that if the initial structure is a flux rope with a footpoint separation distance of S_f, then the height Z_{max} at which the acceleration measured at the centroid of the apex reaches maximum scales with S_f. The primary source of prominence data is the radio data from the archive of the Nobeyama Radio Observatory. A number of Hα events are also included. For CMEs, previously published events with good coverage of the initial acceleration are used. For each event, observed quantities are used to determine S_f and Z_{max}. It is shown that for the events included in the present study, Z_{max} scales with S_f in accordance with the scaling law. The result is consistent with the hypothesis that the pre-eruption magnetic structure underlying a CME and the associated EP is a flux rope driven by the toroidal Lorentz hoop force. The scaling law may constitute a quantitative observable discriminator of the pre-eruption magnetic geometry underlying CMEs/EPs and the driving force.

Subject headings: Sun: Corona; coronal mass ejections; eruptive prominences; observations; CME initiation; MHD

1. Introduction

Since its discovery (Tousey 1973), the phenomenon of coronal mass ejections (CMEs) has been a major scientific issue in solar and heliospheric physics (see, for example, Hundhausen [1999] for a review). Observed in white light, CMEs are often seen to exhibit a 3-part morphology, consisting of a relatively bright rim encircling a relatively dark cavity, which often but not always contains a bright core (Illing and Hundhausen 1986). It is presumed that the core is the white-light counterpart of an eruptive prominence (e.g., Munro et al. 1979; House et al. 1981). Eruptive prominences (EPs) are historically observed in Hα but are also detected by radio telescopes. All of these observing techniques yield two dimensional (2-D) line-of-sight integrated projections of three dimensional (3-D) structures. In addition, while CMEs and EPs are assumed to be driven by magnetic forces, coronal magnetic fields have not been measured to date. As a result, the 3-D magnetic geometry of observed erupting structures remains a major open question. Although CMEs and EPs are closely associated, the precise structural relationship between CMEs, associated EPs, and the underlying magnetic structure is also not yet clearly established.

†Now at K.U.Leuven and Royal Observatory of Belgium, Avenue Circulaire 3, B-1180 Brussels, Belgium

Theoretically, a CME has been hypothesized as the eruption of a pre-existing magnetic flux rope (Chen 1989; Chen and Garren 1993; Chen 1996; Wu, Guo, and Dryer 1997; Gibson and Low 1998; Krall et al. 2001; Roussev et al. 2003). Another concept assumes that an initial magnetic arcade evolves into a magnetic flux rope during the eruption process via macroscopic reconnection (e.g., Antiochos et al. 1999; Chen and Shibata 2000; Amari et al. 2000; Linker et al. 2001; Cheng et al. 2003). These studies all indicate that magnetic flux ropes (MFRs)—or simply flux ropes—play an important role in CME-EP eruptions. However, precisely when and how an MFR comes into play is an unanswered question to be addressed in the present paper.

Key observational support for the flux rope hypothesis comes from direct comparisons of theory and data showing that observed CME dynamics can be explained in terms of the calculated dynamics of expanding flux ropes (Chen et al. 1997, 2000; Wood et al. 1999; Krall et al. 2001; Chen and Krall 2003) with the theoretical results given by the erupting flux-rope CME model of Chen (1996). The erupting magnetic structure is driven by the Lorentz self-force, the so-called hoop force, acting on a flux rope with fixed footpoints (Chen 1989). In addition, the morphological properties obtained from synthetic coronagraph images of flux ropes are in good agreement with observed limb and halo CMEs (Chen et al. 2000; Krall et al. 2006). Detailed morphological considerations also indicate that expected geometrical properties of MFRs are exhibited by observed CMEs (Dere et al. 1999; Plunkett et al. 2000).

The magnetic geometry of the eruptive structure is of fundamental importance in understanding the dynamics of CMEs because Lorentz force acting on a magnetized structure critically depends on the 3-D configuration of the electric current $\mathbf{J}$ and magnetic field $\mathbf{B}$. Although magnetic field in the corona is not directly measurable at the present time, there are observable signatures in the CME dynamics that are characteristic of the flux-rope geometry. Chen and Krall (2003), hereafter Paper 1, theoretically derived a scaling law for the acceleration of CMEs: if the pre-eruption structure is a MFR with the footpoints separated by a distance of S_f, then there exist two critical heights that scale with S_f, given by $Z_* = S_f/2$ and $Z_m \simeq 1.5 S_f$, such that the height Z_{max} where the acceleration of the centroid of the apex of the flux rope is maximum satisfies $Z_* < Z_{max} < Z_m$. The specific value of Z_{max} is determined by precisely how the flux rope is driven. The two critical heights are analytically derived from the equations of motion for flux ropes under the action of the toroidal Lorentz force (Chen 1989), and the footpoints are defined at the base of the corona. This scaling law is universal in that it only depends on the toroidal flux-rope geometry with fixed footpoints and the nature of the Lorentz force but is not dependent on the speed of eruption, the magnitude of acceleration, or the size and mass of the flux rope.

Paper 1 also identified two phases of acceleration distinguished by various contributions to the net accelerating force: the main acceleration phase corresponds to $Z < Z_m$ where Lorentz force dominates and the residual acceleration phase to $Z > Z_m$ where the Lorentz and other competing forces such as gravity and drag force are comparable, all decreasing with height. Subscript "m" refers to the main acceleration phase. Noting that $Z_* \propto S_f$ and $Z_m \propto S_f$, we see that the main acceleration phase is governed by the scale length S_f. This phase corresponds to the "impulsive acceleration" phase empirically defined by Zhang et al. (2004). The time scale of eruption was also discussed in Paper 1 but will not be considered in the present paper.

The significance of establishing the scale lengths in the observed CME acceleration is that in constructing a physical model, the scales constrain the macroscopic geometry of the underlying structure and the accelerating force acting on it. For example, in a magnetohydrodynamic (MHD) description of the macroscopic motion, the intrinsic scales are not set by the equations themselves but by the geometry under consideration that is imposed by the model construct.

In Paper 1, the scaling law was tested against three CMEs whose main acceleration phases were well resolved by the C1 and C2 instruments of the Large Angle and Spectrometric Coronagraph (LASCO) on board the Solar and Heliospheric Observatory (SOHO) (Brueckner et al. 1995). In addition, the flux rope properties were inferred for two Hα EPs described by Vršnak (1990) and Vršnak et al. (1993). These events were found to

be consistent with the scaling law. In the present paper, we further test the flux-rope scaling law by (1) using a larger number of events and (2) using prominences to better estimate S_f of the underlying magnetic flux ropes. We have used 13 EPs and four CMEs for this study. For the prominences, we primarily use the radioheliograph data of the Nobeyama Radio Observatory (NoRH) (Nakajima et al. 1994) and have chosen events where the legs can be observed. We also use Hα prominence events observed by the Big Bear Solar Observatory (BBSO) and Kanzelhöehe Solar Observatory (KSO), which are part of the global high-resolution Hα network (Steinegger et al. 2000).

We treat a CME and the associated EP as different parts of a flux rope with specific assumed geometrical relationships among the CME, EP, and flux rope, which will be referred to as the CME-EP-MFR system. This approach provides a unified theoretical framework of the CME-EP-MFR system. Thus, the work reported in the present paper constitutes a quantitative test of these geometrical assumptions as well as the scaling law itself. We will demonstrate that the flux-rope scaling and the geometrical assumptions underlying the CME-EP-MFR structure are in good agreement with the data.

The remainder of the paper is organized as follows. In section 2, we describe the specific geometrical assumptions of the CME-EP-MFR system including the structural relationships between observed EP features and the MFR. The physics of the scaling law is also briefly reviewed. Section 3 describes the data, the data analysis method, and the results of comparing theory with data. The physical implications of the results are discussed in section 4. Section 5 provides a summary.

2. Magnetic Geometry and the Flux-Rope Scaling Law

2.1. Geometry of the CME-EP-MFR System

Figure 1 shows a schematic drawing of a magnetic flux rope. The electric current **J** is localized to a current channel of major radius R and minor radius a (the toroidal loop structure shown), with components J_t and J_p in the toroidal (locally axial) and poloidal (locally azimuthal) directions, respectively, as indicated on the right. The magnetic field **B** of the flux rope, given by $\mathbf{J} = (c/4\pi)\nabla \times \mathbf{B}$, has poloidal component B_p and toroidal component B_t, as indicated on the left. The toroidal field is confined to the current channel, but the poloidal field can extend beyond. A helical field line inside the current channel and some poloidal field lines outside the current channel are illustrated. Coronal magnetic field B_c due to currents unrelated to **J** is shown in the poloidal direction. The poloidal field B_p inside the current channel is characteristically stronger than B_c with $B_p/B_c \sim \mathcal{O}(R/a)$ (Chen 1989). By a flux rope, we refer to the current and the magnetic field of the system, including the poloidal field B_p outside the current channel (but not B_c).

In Figure 1, the centroid of the apex is at height Z from the photosphere, and the footpoints of the flux rope are separated by distance S_f, measured center to center. The arrow marked Z on the left points to the centroid. Each footpoint has current-channel minor radius a_f, and we will use a_a to denote the minor radius at the apex. The angular position θ along the flux rope is measured from a footpoint, denoted by $\theta = \theta_f$. Here, we take the footpoints to be defined at the base of the corona. The transition to the photosphere is not included in the model except that the total current is taken to be conserved. The model assumes that a_f and S_f are constant. The prominence is indicated by the short vertical line segments with the footpoints separated by S_p at the base of the corona (dashed double arrow). Coronal pressure p_c is also indicated. The Lorentz force and pressure gradients across the flux rope minor radius contribute to a major radial force F_R acting on the current channel, illustrated in Figure 1 in the outward pointing direction. Gravity and drag affect the dynamics (Chen 1989) but do not concern us in the present analysis.

We also assume that the current channel initially has uniform minor radius, i.e., $a(\theta, t = 0) = a_f$ for all θ between the two footpoints. This assumption is not necessary but simplifies the analysis and is valid if the initial flux rope lies lower than one gravitational scale height in the corona, which is $H_g \equiv 2kT/m_i g \simeq 10^5$ km in the lower corona, where k is the Boltzmann constant, m_i is the ion mass, and g is the gravitational acceleration at the solar surface. As the flux rope expands, a_f remains constant but a_a expands, with

$a(\theta)$ monotonically increasing from a_f to a_a at the apex. This is essential for correctly describing the dynamics of an erupting flux rope (Chen and Garren 1993).

While the CME-EP-MFR geometry shown in Figure 1 was used in Paper 1 to analyze two EPs, the quantitative relationship between the prominence and the underlying flux rope was not published. Here, we provide the details, which will be used to analyze the data and interpret the results.

Based on physical considerations, the outer boundary of the flux rope is taken to be at minor radius $2a(\theta)$ from the axis of the flux rope (Chen et al. 1997). Thus, when viewed "end-on", the bright rim of a CME corresponds to the projection of the apex with width $D = 4a_a$. In Figure 1, this viewing perspective is indicated by the short arrow on the right. In this figure, poloidal field lines at $2a(\theta)$ are drawn at three different θ positions along the current channel. According to this geometrical identification, the bright leading edge (LE) of a CME is at height

$$Z_{LE} = Z + 2a_a \tag{1}$$

from the photosphere (arrow marked Z_{LE} in Figure 1). Following Chen (1996), we assume that the prominence material is "dragged along" by the relatively strong magnetic field inside the current channel and identify the prominence with the inner edge of the flux rope. Then, the centroid of the apex of the flux rope and the apex of the prominence are related by

$$Z_p = Z - a_a. \tag{2}$$

This height is also indicated by an arrow marked Z_p on the left. These geometrical assumptions are broadly consistent with the fact that the trajectory of an EP can be extrapolated to that of the associated white-light feature behind the CME rim observed higher in the corona (e.g., Illing and Hundhausen 1986; Gopalswamy et al. 2003). Throughout the paper, subscript p will be used to denote prominence quantities. By height of the apex or flux rope, we will refer to Z, the height of the centroid.

If the prominence material can be identified with the inner edge of the current channel throughout the flux rope, the separation distance S_p between the prominence footpoints and that of the flux rope footpoints S_f are related by

$$S_f = S_p + 2a_f. \tag{3}$$

(See arrows S_f and S_p in Figure 1.) We adopt the idealization that during expansion, the flux rope maintains a toroidal geometry with stationary footpoints. By toroidal, we mean that the flux rope can be locally approximated as a segment of a torus of variable minor radius, not a complete torus. We make the further simplification that the toroidal axis of the flux rope is a circular arc so that the major radius and the apex height have a simple relationship

$$R = \frac{Z^2 + S_f^2/4}{2Z}. \tag{4}$$

Figure 2a illustrates the CME-EP-MFR geometry with a CME observed by LASCO/C2 on 2000 September 12. The CME consists of a relatively bright, smoothly organized rim, a dark cavity indicated by an arrow on the right, and a bright prominence (P). The morphology of the CME is consistent with a flux rope viewed approximately from the side, as depicted in Figure 1, but oriented slightly obliquely with respect to the plane of the sky (strikingly similar to the view shown in Figure 2 of Chen [1996]). Accordingly, the nearly circular cavity at right and the surrounding relatively bright rim are identified as an oblique projection of the minor cross-section. It is noteworthy that the entire CME is considerably larger than the prototypical three-part structure per se. See Chen et al. (2000) for a detailed discussion of a similar CME morphology.

Figure 2b shows an image of the source region obtained by the Extreme Ultraviolet Imaging Telescope (EIT) on board SOHO (Delaboudiniére et al. 1995), taken at 195 Å. At this wavelength, the event is seen as an EP. The filament, appearing as a dark absorbing feature in this image, is shown shortly after its eruption. The two footpoints of the prominence are indicated by $F1$ and $F2$. They are identified by the essentially stationary legs observed in successive images. The midpoint between the two footpoints is indicated by point O. This event was also observed by the KSO in Hα and has been discussed by Vršnak et al. (2003), Qiu et al. (2004), and Schuck et al. (2004). For this event, the height-time data from various

instruments (EIT, Hα, and C2) indicate that the prominence structure seen in C2 corresponds to that observed in the EIT image. The geometrical relationship between the prominence and the rim is also maintained throughout the event observed by C2 and C3.

Recalling that the bright rim encircling the cavity has radius $2a$, we identify the widest extent of the dark cavity (measured vertically in this image to minimize projection effect) as $D = 4a$, and the toroidal axis of the flux rope is taken to go through the center of the cavity. The LE of the apex, which is seen nearly due south of Sun center in Figure 2a, is at height Z_{LE} so that the centroid height is $Z = Z_{LE} - 2a$ using equation (1). For this event, we are also able to obtain the height of the prominence apex $Z_p(t)$ in the C2 as well as in the EIT field of view. There is, however, no direct means to determine S_f for the flux rope. Instead, we can measure the prominence footpoint separation S_p or the length of the pre-eruption prominence.

In determining prominence and CME heights, we assume that an eruption occurs in such a way that the apex velocity is normal to the surface at the midpoint between the footpoints (e.g., point O in Figure 2a). All measured heights given in this paper such as Z, Z_{LE}, and Z_p are true heights with the projection effects accounted for accordingly ("deprojected").

Although the C2 images of this event show the prominence in relation to the rest of the CME, we do not have measurement of Z_{LE} at the earliest times, and observations of a prominence alone do not directly yield the flux-rope quantities a_f, S_f, $a_a(t)$, and $Z(t)$. Instead, we use equations (2)–(4) to calculate a_f, $a_a(t)$, S_f, and $Z(t)$ from measured S_p and $Z_p(t)$ based on the geometrical assumptions, as follows.

Defining

$$\alpha(t) \equiv \frac{R}{a_a(t)}, \tag{5}$$

we re-write equation (4) as

$$2\alpha(Z_p + a_a)a_a = (Z_p + a_a)^2 + \frac{1}{4}(S_p + 2a_f)^2. \tag{6}$$

In this equation, a_f and α are not observed.

For $\alpha(t)$, we make use of a theoretical property of erupting magnetic flux ropes that the variation in α during the main acceleration phase is limited. This property is illustrated in Figure 3. The top panels show the acceleration-time profiles of three LASCO CMEs previously discussed in Paper 1. The C1-C2-C3 data points are given by diamonds. The solid and dashed curves show the theoretical acceleration profiles for the LE and the centroid, respectively, obtained using the model equations of Chen (1996). For each event, the vertical dashed line marks the transition from the main acceleration phase to the residual acceleration phase: the main acceleration phase is to the left, and the residual acceleration phase is to the right (Paper 1). We have reexamined these solutions and calculated the value of α for each event. The middle panels show α versus time. During the main acceleration phase of each event, α is relatively constant in spite of the rapid rise and fall of the acceleration. For the first event, α varies from ~ 2.5 to ~ 4 in the main acceleration phase, with a minimum at ~ 2. It continues to increase beyond the main phase until a plateau is reached, but only values during the main phase are relevant to the present analysis. For the second event, α also starts out at about ~ 2.5, dips to ~ 2, and then increases to ~ 2.7. The third event has an even more constant α, starting with ~ 2.5 and ending with ~ 2.2, after dipping to ~ 1.9. These three flux ropes are representative of a range of acceleration, from tens of m s^{-2} up to several hundred m s^{-2}. Similarly, we have re-analyzed the model results for the 11 LASCO events studied by Krall et al. (2001) and calculated α for the published solution for each event. Specifically, we find that values of α averaged over the main acceleration phase are in the range of ~ 1.7 to ~ 3.3 for the best-fit solutions for these events, with most values in the range of 2 to 2.5. In the most extreme case of the 11 events, which is also the most impulsive case, α varies by $\pm$ 25 % during the main acceleration phase. The average value for the 11 events is

$$\overline{\alpha} = 2.3 \pm 0.3. \tag{7}$$

Note that the near constancy of α is related to the nearly constant aspect ratio $\Lambda \equiv (Z + R_\odot)/D$ that has been found in all of the flux-rope CMEs analyzed (Krall et al. 2001; also see Chen et al. 1997, 2000; Wood et al. 1999). Thus, this assumption of nearly constant α is supported by observations. Here, $D = 4a$ is the minor diameter or width of the apex. Clearly, α is not strictly constant, but its variation is typically limited during

the main acceleration phase. The bottom panel for each event shows various quantities that determine the actual acceleration-time profiles and will be discussed in the next section.

In the remainder of the paper, we will treat α as a known constant and set it to $\alpha = 2.3$ but account for its variations in the uncertainty of the results. We can now obtain a_f and $a(t)$. To find a_f, we solve equation (6) at $t = 0$ by setting $a_a = a_f$ and $Z_p = Z_{p0}$. Solving the algebraic equation for a_f, we find

$$a_f = \frac{1}{4(\alpha-1)}\Bigg[S_p - 2(\alpha-1)Z_{p0} + \Big\{[2(\alpha-1)Z_{p0} - S_p]^2 + 2(\alpha-1)(4Z_{p0}^2 + S_p^2)\Big\}^{1/2}\Bigg], \tag{8}$$

where Z_{p0} and S_p are the measured initial height and the constant footpoint separation distance of the prominence, respectively. For a_a at time $t > 0$, we substitute a_f in equation (6) and obtain the minor radius at the apex,

$$a_a(t) = \frac{1}{2\alpha-1}\Big\{(\alpha-1)^2 Z_p^2(t) + (2\alpha-1)[Z_p^2(t) + \frac{1}{4}(S_p + 2a_f)^2]\Big\}^{1/2} - \left(\frac{\alpha-1}{2\alpha-1}\right) Z_p(t). \tag{9}$$

Equations (8) and (9) provide estimates of a_f and $a_a(t)$ for the unobserved flux rope that contains an observed prominence. Using the measured S_p and calculated a_f, we obtain S_f from equation (3). Using the measured $Z_p(t)$ and calculated $a_a(t)$, we obtain $Z(t)$ from (2).

2.1.1. The Flux-Rope Scaling Law

Paper 1 presented a new scaling law that governs the main acceleration phase for erupting flux ropes: if an initial flux rope with fixed footpoint separation of S_f expands under the action of the Lorentz hoop force, the acceleration profile exhibits two critical heights Z_* and Z_m that scale with S_f, given by

$$Z_* = \frac{S_f}{2} \tag{10}$$

and

$$Z_m \simeq 3Z_* = 1.5S_f. \tag{11}$$

Physically, Z_* is the height of the apex where the flux rope is semi-circular so that the major radial curvature

$$\kappa \equiv \frac{1}{R}$$

is maximum. This is purely a geometrical property of a toroidal flux rope with constant S_f. The accelerating hoop force is proportional to κ^2, and with other factors affecting the force, the acceleration reaches maximum when the apex height is somewhat higher than Z_*. The critical height Z_m is defined to be the apex height where the centroid acceleration decreases to approximately 1/4 of the peak value. The apex height Z_{max} where the actual acceleration maximum is attained is determined by the details of the initial system and how the poloidal flux varies and satisfies

$$Z_* < Z_{max} < Z_m. \tag{12}$$

The derivation of the scaling law and the underlying physics of CME acceleration are based on the Lorentz force acting on a toroidal flux rope as depicted in Figure 1 and are given in Paper 1. Below, we summarize the relevant physics of the flux-rope scaling law of CME acceleration.

The acceleration of the apex under the action of the Lorentz hoop force can be written as

$$\frac{d^2Z}{dt^2} \sim k_R^2(t)\Phi_p^2(t)f_R(t), \tag{13}$$

where

$$k_R^2(t) \equiv \frac{1}{[R\ln(8R/a_f)]^2} = \frac{\kappa^2}{[\ln(8R/a_f)]}.$$

The function $\Phi_p(t)$ is the poloidal flux of the flux rope, and $f_R(t)$ is a function that depends on the details of the contributions to the net force as the flux rope expands. Both functions increase with time to some finite values, with $f_R(t = 0) = 0$ if the initial flux rope is in equilibrium, except that f_R may decrease slightly for $t \simeq 0$. From equation (4), it is easy to analytically show that both k_R and κ are maximum at $Z = Z_*$, given by $dk_R/dZ = 0$ and $d\kappa/dZ = 0$, respectively.

For a given initial flux rope, however, the actual height of maximum acceleration, Z_{max}, is where the product of the three quantities, $k_R^2(t)$, $\Phi_p^2(t)$, and $f_R(t)$ reaches maximum. Because the latter two are increasing functions, we have $Z_{max} > Z_*$.

The bottom panels of Figure 3 show these functions for three events. For each event, the dashed curve in the top panel is the product of the three functions shown in the bottom panel. We see that the actual maximum acceleration heights are greater than Z_*.

Above Z_{max}, the acceleration decreases rapidly with increasing height because $k_R^2 \sim [R\ln(R/a_f)]^{-2}$, quenching the acceleration regardless of the detailed form of $\Phi_p(t)$ and $f_R(t)$ for any reasonable physical systems. The acceleration decreases to approximately 1/4 of the peak value when the apex reaches $Z \simeq Z_m$. The actual height of maximum acceleration, determined by the product of k_R^2, $\Phi_p(t)$, and $f_R(t)$, satisfies the inequality (12) (see a detailed discussion in Paper 1). Note that it is R/a_f, rather than R/a_a, that occurs in k_R. This is significant because $R/a_a = \alpha$ remains of order unity whereas $R/a_f \gg R/a_a$ as the flux rope expands. Noting $\ln(R/a_f) = \ln(R) - \ln(a_f) \simeq \ln(R)$ for $R \gg a_f$, we see that $k_R^2 \sim [R\ln(R)]^{-2}$ decreases much faster than R^{-2}, which would be the case if $k_R \sim 1/R\ln(R/a_a)$. This property of k_R and therefore the observed rapid decrease in the main acceleration is traced to the form of the inductance of the expanding flux rope (Chen and Garren 1993), which is elaborated on in Paper 1. This inductive property was not accounted for in the original formulation (Chen 1989).

Note that the critical height Z_* is purely a geometrical property of a flux rope with fixed footpoints derivable from equation (4), while Z_m arises from the Lorentz force acting on a toroidal flux rope, which gives rise to the factor k_R^2 in the acceleration discussed above. These critical heights do not depend on the speed of eruption, the magnitude of acceleration, or the size and mass of the underlying flux rope. As such, the scaling law is universal. In the present paper, we will test the main tenet of the scaling law, inequality (12), against the sample of EPs and CMEs. In applying the theoretical results, it is important to keep in mind that the scaling law, (10)–(12), refers to MFR quantities, such as S_f and Z_{max}, rather than prominence quantities such as S_p and Z_p.

3. Observational Data and Results

3.1. Observations

The prominence events used in the present paper were mainly selected from the NoRH data archive during a visit of one of the authors (A. V.) to the Nobeyama Radio Observatory. The radio observations were taken at 17 GHz. Maps were synthesized in both stokes I and V using the Steer algorithm at 3 or 5 min cadence. The resolution of the CLEANed maps is 4.91 arcsec/pix. The height-time measurements were made on the Stokes I maps. A total of seven prominence events are used from this NoRH data set that clearly show the prominence legs and yield enough height-time data points to determine the acceleration during the main acceleration phase. One of these events was recently described by Kundu et al. (2004). We have also included Hα events from the BBSO and KSO data sets as well as the events previously analyzed by Vršnak (1990) and Vršnak et al. (1993). For the EP events used in the present paper, we also examined the LASCO C2/C3 and EIT counterparts, where available. For CMEs, the LASCO C1-C2-C3 data did not yield a large number of usable events because of lack of high-cadence C1 data, which would be needed to resolve the acceleration peaks of typical CMEs. Thus, we included the three LASCO C1-C2-C3 events from Paper 1 and one event whose initial acceleration was observed by Mark III (MK3) coronameter of Mauna Loa Solar Observatory. This event (1997 September 9) was previously discussed by Chen et al. (2000).

The measurements for EP (radio, Hα, EIT data) and CME height-time as well as those for footpoint positions were made using standard computer software developed for the analysis of LASCO and EIT data. The successive positions of the LE of CME and of the eruptive filament were recorded approximately at the same position angle from the low corona (LASCO/C1, NoRH, EIT, Hα, or MK3) to the outer corona (LASCO C2/C3). The instantaneous velocity and the acceleration profiles were then obtained by computing successively the first and second derivatives of the height-time curve. The heights of maximum acceleration Z_{max} were then determined from the acceleration-height curves. In order to resolve the acceleration peak, we chose events observed with

highest possible time-cadences up to one image every 3 minutes for EPs (in Hα or radio).

As mentioned earlier, the scaling law refers to the true height above the photosphere. All measured heights given in this paper are deprojected.

3.2. Analysis of Data

In this section, we describe our methodology and analysis of data. For the 2000 September 12 event (event 4) shown in Figure 2, we obtained the heliographic coordinates of the footpoints observable in EIT, finding $F1$ = (E6°, S24°) and $F2$ = (W23°, S17°) with the midpoint (point O) at (W8°, S20°), yielding a prominence footpoint separation distance $S_p = 0.48R_\odot$. The estimated initial deprojected height of the prominence is Z_{p0} = 0.1 $R_\odot$. This EP event was measured using both EIT and KSO Hα data. The prominence attained its maximum acceleration at $Z_{p,max} = 0.91R_\odot$, where $Z_{p,max}$ is the measured height of maximum acceleration of the prominence apex. Using equations (8) and (9) in conjunction with equations (2) and (3), we find $S_f = 0.90R_\odot$ and $Z_{max} = 1.21R_\odot$ for the underlying flux rope. Here, we have assumed that $Z_p = Z_{p,max}$ and $Z = Z_{max}$ occur at the same time. This introduces a small error ($Z_{p,max}$ usually occurs slightly earlier), which will be neglected.

As another example, Figure 4a shows an EIT 304Å image of an eruptive prominence associated with a CME, taken at 0719 UT on 1999 September 14 (event 3). By examining the sequence of images leading up to this time, we determined that one footpoint can be traced to the brightening, A. The second leg intersects the west limb at B (latitude ∼N28°). The actual footpoint had moved beyond the limb approximately one to one and a half days previous to this time. The apex of the prominence is marked by C. Figure 4b shows an EIT 195Å image of the presumed source region taken approximately one week earlier. By running the "movie" backwards in time, we identified the features marked by $F1$ and $F2$ as the locations corresponding to A and B, respectively. The heliographic coordinates of $F1$ and $F2$ are $F1$ = (E23°, N43°) and $F2$ = (W18°, N28°). This yields $S_p = 0.63R_\odot$ as the footpoint separation distance. The eruption occurred essentially on the west limb (W90°), with the initial prominence height at $Z_{p0} = 0.11R_\odot$ and peak-acceleration height of $Z_{p,max} = 0.35R_\odot$. Using equations (8) and (9) and equations (2) and (3), we find $S_f = 1.16R_\odot$ and $Z_{max} = 0.60R_\odot$.

In determining S_f, we use the linear distance between the two points, neglecting the curvature of the solar surface. For very large footpoint separation distances, say, $S_f > 1R_\odot$, the curvature of the solar surface can affect the forces because electric currents are presumably induced in and near the surface as poloidal flux is injected into the flux rope. This effect is not included in the model. However, it does not affect the fact that the flux-rope curvature is maximum at centroid height $Z = Z_*$.

Figure 5 illustrates the different stages of one filament eruption and its associated CME as seen by NoRH and LASCO on 2003 February 18 (event 9). All four panels are displayed in reverse video, which means that bright sources in radio and white-light (in the fourth panel) are shown as dark areas in this figure. The first three panels are NoRH radioheliograms obtained at 17 GHz, each one showing an aliased image of the Sun on the upper right corner. This is an artifact and depends on the antenna spacing and the actual position of the Sun in the sky at the time of the observations. The upper left panel is a pre-eruption image showing the filament (arrows) as a brightness depression on the quiet Sun. At 17 GHz, the chromosphere and filaments are optically thick, which means that their brightness temperature is close to the local electron temperature. Being cooler than the surrounding chromosphere, filaments typically appear in absorption on the disk and in emission when observed above the limb. The next two panels illustrate this behavior where a part of the filament is still on the disk during the eruption. The fourth panel is a LASCO-C2 image showing the early development of the associated CME that exhibits a typical 3-part structure, with a front, a well defined cavity, and the prominence (arrow).

To accurately determine the footpoint separation distance S_p for the EPs observed by NoRH including this one, we used EIT images, where available, as illustrated in Figure 2. For one backside event (2002 February 18, event 7), we used Hα data.

Although the method is straightforward, there are errors and uncertainties in measuring footpoint positions and heights. Tracking a given fea-

ture such as the LE to determine its speed and acceleration—particularly if multiple instruments at different wavelengths are used—introduces uncertainties. The resulting velocity and especially the acceleration curves may contain significant errors or gaps. To mitigate this problem, the height-time measurements are first interpolated onto an evenly spaced time grid with a resolution identical to the smallest time resolution available (from NoRH or EIT). These measurements are then convolved with a low pass filter in order to get smooth variations. Figure 6 illustrates this method for the filament eruption shown in Figure 5 (event 9). The top panel is a height-time plot for the prominence observed by the NoRH and LASCO-C2 (open circles) and the LE of the corresponding CME by LASCO-C2 and C3 (solid circles). The approximate field of view of C2 is indicated by the two horizontal dashed lines. The lower two panels present the instantaneous velocity and the acceleration, respectively, versus height. The open circles are the speed or acceleration deduced from the raw unfiltered height measurements, which in this event are moderately noisy, as indicated by the error bars. Dashed line segments are used to connect the circular data points. During the first two hours of the data, the filament height remains roughly constant (first panel), and the corresponding data points are clustered at $\sim 1\ R\odot$ in the lower two panels. The dash-dot curves are obtained using re-interpolated data (3-minute time resolution for this event), and the solid curves are calculated using the filtered data. For each of the filament eruptions in this study, we checked the consistency of the acceleration peak obtained from the raw data and the filtered ones. For the EPs studied by Vršnak (1990) and Vršnak et al. (1993), we used the published measurements of S_p, Z_{p0}, and $Z_{p,max}$. For event 6, we used the height-time data and S_p obtained by Kundu et al. (2004) and used the method described here to obtain Z_{max}.

For CMEs, we have used observational proxies such as neutral line or filament channel lengths to estimate S_f. The height of maximum acceleration Z_{max} is determined by following the midpoint of the widest transverse span of the bright rim. This method was used in previous papers comparing theory and CME observation (Chen et al. 1997, 2000; Wood et al. 1999; Paper 1).

The EP and CME events and their properties are listed in Tables 1 and 2, respectively. In Table 1, S_p, Z_{p0}, and $Z_{p,max}$ are prominence quantities obtained from the data while S_f and Z_{max} are the quantities of the underlying flux rope deduced using equations (8) and (9). For CMEs (Table 2), S_f and Z_{max} are determined from the data.

3.3. Results

Figure 7 shows the results plotted as Z_{max} versus S_f for the 17 events, encompassing a wide range of size and eruption speed. The horizontal axis S_f is determined by the appropriate method for each event, and the vertical axis is Z_{max}, the height at which the centroid of the flux rope is determined to attain maximum acceleration. The data for EP events are shown as solid circles, and CME events as open triangles. The straight line A is defined by $Z_{max} = Z_* = S_f/2$, and line B, the upper bound of the main acceleration phase, is $Z_{max} = Z_m$. For this plot, we have used $Z_m = 1.5S_f$. In accordance with inequality (12), an event that obeys the flux-rope scaling law falls between A and B, the exact position being dependent on the details of the driving force [i.e., the form of $\Phi_p(t)$]. The estimated error bars, to be discussed further in the next section, are presented. The figure shows that the CME-EP events in this sample are consistent with the scaling law for the full range of S_f values, with no statistically significant deviations.

The 2002 February 18 EP (event 7) falls outside the range $Z_* < Z_{max} < Z_m$. This event occurred on the backside of the Sun, observable as a southern limb event near the pole. As such, it might be excluded from the sample because it is impossible to determine the footpoints. However, we include it to illustrate how such uncertainties are manifested in the plot. We estimate S_p for this event by examining Hα images about two weeks prior to the event, identifying a high-latitude candidate prominence. Figure 8 shows an image taken on 2002 February 4. The footpoints $F1$ and $F2$ are indicated in the image, with the separation distance $S_p = 0.43R_\odot$. It is also possible, however, that the footpoints of the eruptive structure were $F1$ and $F2'$, in which case we obtain $S_p = 0.62R_\odot$. Thus, the determination of S_p may be uncertain by 50% or possibly more for this event. In Figure 7, we have given the result of using $S_p = 0.43R_\odot$ as event 7 and $S_p = 0.62R_\odot$ as event 7'. These

two points provide an idea of the error in the determination of S_f due to the inability to ascertain the locations of the footpoints in this case.

Figure 5 shows that event 9 was a partial prominence eruption: the entire length of the filament did not erupt at the same time. The curvature κ of the flux rope is determined by the effective footpoints of the part that erupts. Thus, in this case, the entire length of the filament would significantly overestimate S_f. For this particular event, the rest of the filament did erupt later. We have used the apparent footpoints as shown in the third image of the eruption. This is an example where the full length of the filament or neutral line alone would be an inaccurate proxy for S_f.

For event 6, Kundu et al. (2004) provided a detailed description of the eruptive prominence and the associated fast CME. Using the NoRH radio data, they were able to measure the height of the EP. In addition, they determined the prominence footpoint separation distance to be $S_p \simeq 390'' = 0.39R_\odot$. The maximum prominence acceleration was found to occur at $Z_{p,max} \sim 0.26R_\odot$. Identifying the prominence itself as a flux rope, they concluded that $Z_{p,max} > S_p/2 = 0.20R_\odot$. Applying our method to the data, we obtained $Z_{p,\,max} \simeq 0.5R_\odot$ and $Z_{p0} \simeq 0.08R_\odot$. Using these values and $S_p = 0.39R_\odot$ in (8) and (9), we obtained the flux-rope quantities $S_f \simeq 0.7R_\odot$ and $Z_{max} \simeq 0.69R_\odot$. This yields $Z_* \simeq 0.35R_\odot$ and $Z_m \simeq 1.05R_\odot$, satisfying the scaling law (12). This event falls in the middle between lines A and B as shown in Figure 7.

The derivation of the scaling law assumes $Z_0 < Z_*$ so that the curvature κ of the initial configuration is less than that at Z_*. If the initial structure has $Z_0 > Z_*$, the scaling law is inapplicable because κ monotonically decreases with height for $Z > Z_*$. If a given event has $Z_0 > Z_*$, it may or may not fall between lines A and B, but an ensemble of such events would show a statistically different distribution. We did not find an example of this situation in our data set.

Note that $\alpha \simeq 2$ corresponds to a relatively "fat" flux rope. Table 1 shows that some initial flux ropes are located so low that $Z_0 - 2a_a < 0$. This means that the outermost flux surfaces may be partially in the chromosphere or even in the photosphere, or that the minor cross-sections may be deformed. In addition, the assumption $a_a(t = 0) = a_f$ for the initial flux rope may not be strictly valid if $Z_0 \gg H_g$, the gravitational scale height. The theory does not include these complications. Moreover, the basic equations are strictly valid for slender flux ropes, $R/a \gg 1$ (Garren and Chen 1994), with correction terms of $\mathcal{O}(a/R)$. Nevertheless, the scaling law primarily depends on the fact that once eruption starts and the flux rope begins to rise, the major radial curvature κ is maximum at $Z = Z_*$ and that the Lorentz hoop force is sharply cut off for $R > Z_*$. This fact is not qualitatively altered by these complications. The good agreement evident in Figure 7 supports this assertion.

3.4. Errors

The data points shown in Figure 7 have uncertainties from a number of sources. In estimating the errors, we distinguish two categories. For prominence data, the flux-rope quantities are obtained with the assumption $\alpha = 2.3$ based on the best-fit theoretical solutions for a number of CME events. The statistical error is $\Delta\alpha \simeq 0.3$, which leads to uncertainties in both S_f and Z_{max}. The other category of error is the measurement errors in Z_{p0}, $Z_{p,\,max}$, and S_p. For CMEs, the approximation $\alpha \simeq const$ is not needed and is not used. Rather, S_f, which is not directly observed, is determined from observational proxies as previously described, and Z_{max} is determined from the acceleration-height profiles.

In estimating the errors, we allowed 25% for Z_{p0}, $Z_{p,\,max}$: 10% for measurement and 15% due to uncertainties in the direction of eruption. For S_p, we allowed 20% error for each event. These errors as well as $\Delta\alpha$ for prominences are propagated to the flux-rope quantities S_f and Z_{max} using the standard method by differentiating equations (8) and (9), keeping only the first derivatives. The error due to $\Delta\alpha = 0.3$ roughly accounts for a half of each error bar. The resulting error bars are plotted for each prominence data points. For clarity, error bars are only shown for one CME (event 17).

Note that the error estimation technique assumes that S_f and Z_{max} are independent quantities. In the present work, however, S_f and Z_{max} have dependence on each other via equations (8) and (9). Thus, statistically random errors would not be distributed uniformly in an ellipse defined by the pair of error bars for each data point. Nev-

ertheless, the error bars given in Figure 7 do provide a good indication of the magnitude of uncertainties in the results.

4. Discussion

The fundamental framework of the analytical erupting flux-rope model is provided by MHD as is also the case for simulation studies of solar eruptions (e.g., Wu et al. 1997; Gibson and Low 1998; Antiochos et al. 1999; Chen and Shibata 2000; Amari et al. 2000; Linker et al. 2001; Roussev et al. 2003; Cheng et al. 2003). The MHD equations by themselves generate no intrinsic length or time scales. Instead, scales are determined by boundary conditions, driving mechanisms, and system parameters such as the dimensions of the initial structure and gradients in the background medium. Resistivity and inertia provide additional spatial and temporal scales for dissipative phenomena. In MHD simulations, the finite numerical grid spacing introduces additional scales due to numerics. The evolution of MHD or numerical equations are then governed by these scales.

Paper 1 identified the footpoint separation distance S_f of the initial flux rope as a fundamental length scale that governs the acceleration of a CME-EP-MFR structure. This scale is manifested in CME acceleration profiles as characteristic heights: Z_{max}, Z_*, and Z_m. These heights can be directly determined from data. If the underlying magnetic structure of a CME-EP event is a flux rope prior to the main acceleration phase, then the scaling law (12) should be applicable. The variability in the poloidal flux function $\Phi_p(t)$ produces the spread between the two critical heights Z_* and Z_m. Although there are uncertainties in the observational determination of various quantities, the estimated error bars are less than the difference between the two critical heights (Figure 7).

We briefly discuss the physical significance of the poloidal flux function $\Phi_p(t)$. In one scenario, an increasing $\Phi_p(t)$ corresponds to injection of subphotospheric poloidal flux (or equivalently, magnetic helicity) into a pre-existing flux rope (Chen and Garren 1993; also Chen 1989, 1996). In a fundamentally different scenario, an initial magnetic arcade evolves into a flux rope during the eruption (e.g., Antiochos et al. 1999; Amari et al. 2000; Chen and Shibata 2000; Linker et al. 2001). In such a system, a quantity of coronal magnetic field (B_c in Figure 1) is converted to the poloidal flux of the flux rope, so that $\Phi_p(t)$ increases from an initial value (zero if there is no flux rope at all) to the final value when a flux rope is fully formed. In fact, all models of eruption that ultimately produce flux ropes have quantities that are equivalent to $\Phi_p(t)$. In the former scenario, Poynting flux $\mathbf{S}$ through the solar surface is nonzero (Chen 2001) and determines the form of $\Phi_p(t)$. In the latter class of models, Poynting flux through the solar surface may be zero on the time scale of eruption. If an arcade is transformed into a flux rope early enough in the eruption process, i.e., before the apex rises above the critical height Z_* based on the newly formed footpoints, the scaling should be obeyed. If, on the other hand, flux ropes are formed after the apex has exceeded Z_*, the acceleration profile is governed by the evolving system dimensions and magnetic topology. This, in turn, is determined by macroscopic reconnection. An ensemble of such CME-EP events should show statistically significant deviations from the scaling law. The good agreement between the predicted flux-rope scaling and the data evidenced in Figure 7 implies either that the magnetic structures underlying the observed CMEs and associated EPs are pre-existing flux ropes or that flux ropes are formed prior to the main acceleration phase. In the latter case, the scaling law and the observed CME acceleration profile impose a constraint on the reconnection process. The agreement evident in Figure 7 also implies that the driving force is correctly given by the toroidal hoop force acting on a flux rope with fixed footpoints.

In the MHD simulation model of Roussev et al. (2003), an initial flux rope with fixed footpoints similar to that shown in Figure 1 (without the prominence) is allowed to erupt under the action of the toroidal hoop force. The simulation does not inject flux into the pre-existing flux rope. However, the poloidal flux, equivalent to $\Phi_p(t)$, increases with time because of magnetic reconnection (via numerical diffusion). Although the precise form of the equivalent $\Phi_p(t)$ cannot be determined from the published results, the magnitude of change in $\Phi_p(t)$, occurring on the time scale of reconnection, is expected to be less than

in the examples of Figure 3. Thus, we expect the main acceleration to reach its maximum only slightly above Z_*. With the simulation initial condition $Z_0 = 8 \times 10^4$ km $< Z_* = 9.8 \times 10^4$ km, the scaling law is meaningfully applicable. Substituting into the scaling law the simulation parameter $S_f = 1.96 \times 10^5$ km, the numerical result $Z_{max} \simeq 1.1 \times 10^5$ km is found to be in excellent agreement with the scaling law (also see Paper 1). This simulation result is shown in Figure 7 by the open diamond marked "*s*." Note that Roussev et al. (2003) invoked the equilibrium structure of Titov and Démoulin (1999) as the starting point, an axisymmetric torus with no fixed photospheric footpoints. By virtue of using a partial torus with fixed footpoints, however, the actual simulated system is more consistent with the construct of Chen (1989), yielding the good agreement with the scaling law. This agreement could be more precisely tested by explicitly deriving the quantities $\Phi_p(t)$ and $f_R(t)$ from the simulation model.

As an example of situations where the scaling law does not apply to the observed acceleration, consider CMEs or EPs that exhibit only gradual acceleration at C2 and C3 heights, such as the events discussed by Sheeley et al. (1999) and by Krall et al. (2001) (see their Figures 3, 6d, and 6e). In these cases, the main acceleration phase occurs below the field of view, and the observed acceleration corresponds to the residual acceleration phase (Paper 1) where the net force is determined by the competition of several contributions, all of which are decreasing. Indeed, the measured acceleration profiles given in Sheeley et al. (1999) all show that acceleration was decreasing as the CME entered the C2 field of view.

In deriving the scaling law, the initial flux rope is assumed to be stable to the external kink mode, and the effects of kinking are not included. However, a kinked flux rope is subject to the same toroidal hoop force, so that in an eruption, the dynamics may be governed by the effective footpoints (similar to event 9, Figure 5). Such effects may be investigated using a simulation model of kinked prominences (e.g., Török and Kliem [2005]). Fan and Gibson (2003) simulated a twisted kink-unstable flux tube emerging into a coronal arcade. The model flux rope corresponds to the upper portion of a circular flux rope rising through the photosphere. The simulation shows that it kinks as it rises. In addition, the footpoint separation distance increases slowly with time. Thus, a direct comparison with the scaling law cannot be made. Nevertheless, the flux rope obtains a semi-circular (maximum κ) shape, and the maximum acceleration occurs shortly thereafter. As such, it is consistent with the scaling law to the extent the flux rope dynamics are still governed by the toroidal hoop force. As a general remark, an appearance of kinking in a prominence does not necessarily imply that the flux rope itself undergoes an external kink: the filament constitutes only a small part of the flux rope.

From a practical point of view, the scales—spatial as well as temporal—manifested in observed acceleration profiles can be used to constrain the basic model construct. For example, the flux-rope scaling does not occur in geometries with no footpoints anchored in the Sun such as a straight flux rope (e.g., Forbes and Priest 1995) or a sun-encircling flux rope (e.g., Lin et al. 1998). For a straight geometry, curvature is zero so that the toroidal hoop force is identically zero. A sun-encircling flux rope is driven by the hoop force but has monotonically increasing major radius considerably greater than 1 $R_\odot$, resulting in monotonically decreasing acceleration. Such a configuration would not reproduce the acceleration profile characteristic of the main acceleration phase. This is consistent with the 2.5 dimensional MHD simulation results of Lynch et al. (2004), which are qualitatively consistent with the residual acceleration phase with decreasing acceleration typically exhibited by CMEs at C2 and C3 heights (Sheeley et al. 1999). An interesting unanswered question is what scales may govern the acceleration process in an arcade-to-flux rope model in 3-D, i.e., how the evolving magnetic topology and dimensions are quantitatively manifested in the acceleration profile during the arcade-to-flux rope transformation. We suggest that the scaling law may ultimately provide a discriminator to distinguish between different pre-eruption geometries and accelerating forces.

5. Summary

We have demonstrated that the acceleration profiles of an ensemble of 17 observed CME-EP

events exhibit the theoretically derived flux-rope scaling law. Figure 7 clearly shows that the individual events are bounded within error bars by the two critical heights, Z_* and Z_m, for given footpoint separation distance S_f. The result provides quantitative evidence that the pre-eruption structures were flux ropes or flux ropes were formed before the onset of the main phase for these events.

Physically, the critical height Z_* is determined by the geometrical properties of a flux rope (maximum curvature at apex height of Z_*) while Z_m arises from the nature of the Lorentz hoop force, $d^2Z/dt^2 \sim (R \ln R)^{-2}$ (Paper 1). The fact that the observed acceleration profiles exhibit the scaling law suggests that S_f generally provides a fundamental scale governing the CME/EP acceleration mechanism and supports the concept that CMEs are initial magnetic flux ropes driven by Lorentz hoop force (Chen 1989).

The set of events were chosen according to the requirements that (1) the main phase of the acceleration where the peak acceleration occurs be well observed in the CME or EP data and (2) either a clear observational proxy for the footpoints or the legs of a prominence be clearly identifiable. We have sought to include events with small and large footpoint separations in order to cover the full range of the scaling law. Some possible deviations from the scaling law have been illustrated and explained.

In addition to supporting the flux-rope hypothesis, the good agreement evident in Figure 7 provides a quantitative test of the specific geometrical and structural relationships of the underlying flux rope to the CME LE (equation [1]), prominence apex height (equation [2]), and prominence footpoint separation (equation [3]). These assumptions appear to be valid for the events in this study, and we suggest that they are generally valid.

In the present work, S_f and Z_{max} are computed from data for EPs based on the flux rope hypothesis. However, S_f and Z_{max} in principle can be measured independently of any model assumptions. With improved observations in which S_f and Z_{max} can be directly measured, the scaling law can be definitively tested, and the observed S_f and Z_{max} can then be used as an observational indicator of the magnetic geometry of the pre-eruption structure. This can help resolve the question of when flux ropes are formed and what driving forces are responsible during the main acceleration phase. In this regard, the upcoming STEREO mission may provide observations of CMEs from two vantage points down to about 0.5 $R_\odot$ to resolve the main acceleration phase for CME/EP events.

AV would like to thank Dr. Shibasaki for the invitation to the Nobeyama Radio Observatory and the NoRH staff for the hospitality during his visit. We thank Dr. V. Yurchyshyn for providing the BBSO and KSO data. The LASCO and EIT data used in this work were produced by a consortium of the Naval Research Laboratory (USA), Max-Planck-Istitüt für Aeronomie (Germany), Laboratoire d'Astronomie (France), and the University of Birmingham (UK). SOHO is a project of international cooperation between ESA and HASA. This work was supported by the Office of Naval Research and the National Aeronautics and Space Administration under NNH06AD56I issued through the Office of Space Science.

REFERENCES

Amari, T., J. F. Luciani, Z. Mikić, and J. Linker 2000, ApJ, 529, L49.

Antiochos, S. K., C. R. DeVore, and J. A. Klimchuk 1999, ApJ, 510, 485.

Brueckner, G. E., et al. 1995, Sol. Phys. 162, 357.

Chen, J. 1989, ApJ, 338, 453.

Chen, J. 1996, J. Geophys. Res., 101, 27499.

Chen, J. 2001, Space Sci. Rev., 95, 165.

Chen, J., & Garren, D. A. 1993, Geophys. Res. Lett., 20, 2319.

Chen, P. F., and K. Shibata 2000, ApJ, 545, 524.

Chen, J., & Krall, J. 2003, J. Geophys. Res., 108 (A11), 1410, doi: 10.1029/2003JA009849. (Paper 1)

Chen, J., R. A. Howard, G. E. Brueckner, R. Santoro, J. Krall, S. E. Paswaters, O. C. St. Cyr, R. Schwenn, P. Lamy, and G. M. Simnett 1997, ApJ, 490, L191.

Chen, J., R. A. Santoro, J. Krall, R. A. Howard, R. Duffin, J. D. Moses, G. E. Brueckner, J. A.

Darnell, and J. T. Burkepile 2000, ApJ, 533, 481.

Cheng, C. Z., Y. Ren, G. S. Choe, and Y.-J. Moon 2003, ApJ, 596, 1341.

Delaboudiniére, J.-P., et al. 1995, Sol. Phys., 162, 291.

Dere, K. P., G. E. Brueckner, R. A. Howard, and D. J. Michels, and J. P. Delaboudiniere 1999, ApJ, 516, 465.

Fan, Y., and Gibson, S. E. 2003, ApJ, L105.

Forbes, T. G., and Priest, E. R. 1995, ApJ, 446, 377.

Garren, D. A., and Chen, J. 1994, Phys. Plasmas, 1, 3425.

Gibson, S. E., and Low, B. C. 1998, ApJ, 493, 460.

Gopalswamy, N., Shimojo, J., Lu, W., Yashiro, S., Shibasaki, K., and Howard, R. A. 2003, ApJ, 586, 562.

House, L. L., Wagner, W. J., Hildner, E., and Sawyer, C. 1981, ApJ, 244, L117.

Hundhausen, A. J. 1999, in The Many Faces of the Sun, ed. K. Strong, J. Saba, B. Haisch, and J. Schmelz (New York: Springer), 143

Illing, R. M. E., and Hundhausen, A. J. 1986, 90, 10951.

Krall, J., and Chen, J. 2005, ApJ, 628, 1046.

Krall, J., Chen, J., Duffin, R. T., Howard, R. A., and Thompson, B. J. 2001, ApJ, 562, 1045.

Krall, J., Yurchyshyn, V. B., Slinker, S., Skoug, R. M., and Chen, J. 2006, ApJ, in press.

Kundu, M. R., White, S. M., Garaimov, V. I., Manoharan, P. K., Subramanian, P., Ananthakrishnan, S., and Janardhan, P. 2004, ApJ, 607, 530.

Lin, J., Forbes, T. G., Isenberg, P. A., nd Demoulín, P. 1998, ApJ, 504, 1006.

Linker, J. A., Lionello, R., Mikić, Z., and Amari, T. 2001, J. Geophys. Res., 106, 25165.

Lynch, B. J., Antiochos, S. K., MacNeice, P. J., Zurbuchen, T. H., Fisk, L. A. 2004, ApJ, 617, 589.

Munro, R. H., Gosling, J. T., Hildner, E., MacQueen, R. M., Poland, A. I., and Ross, C. L. 1979, Sol. Phys. 61, 201.

Nakajima, H., Nishio, M., Enome, S. et al. 1994, Proc. IEEE, 82, 705.

Plunkett, S. P., Vourlidas, A., Simberova, S., Karlicky, J., Ktrc, P., Heinzel, Kupryakov, Y. A., Guo, W. P., and Wu, S. T. 2000, Sol. Phys. 194, 371.

Qiu, J., Wang, H. M., Cheng, C. Z., Gary, D. E. 2004, 604, 900.

Roussev, I. I., Forbes, T. G., Gombosi, T. I., Sokilov, I. V., DeZeeuw, D. L., and Birn, J. 2003, ApJ, 588, L45.

Schuck, P. W., Chen, J., and Schwartz, I. B. 2004, ApJ, 610, L133.

Sheeley, N. R., Jr., Walter, J. H., Wang, Y.-M., and Howard, R. A. 1999, 104, 24739.

Steinegger, M., et al. 2000, in The Solar Cycle and Terrestrial Climate, ed. A. Wilson (SP-463; Noordwijk: ESA), 617.

Titov, S. V., and Démoulin, P. 1999, A&A, 351, 707.

Török, T., and Kliem, B. 2005, ApJ, 630, L97.

Tousey, R. 1973, Space Res., 13, 713.

Vršnak, B. 1990, Sol. Phys., 127, 129.

Vršnak, B., Ruždjak, V., Rompolt, B., R0ša, D., and Zlobec, P. 1993, Sol. Phys., 146, 147.

Vršnak, B., Klein, K. L., Warmuth, A., Otruba, W., and Skender, M. 2003, Sol. Phys., 214, 325.

Wood, B. E., Karovska, M., Chen, J., Brueckner, G. E., Cook, J. W., and Howard, R. A. 1999, 512, 484.

Wu, S. T., Guo, W. P., and Dryer, M. 1997, Sol. Phys. 170, 265.

Zhang, J., Dere, K. P., Howard, R. A., and Vourlidas, A. 2004, ApJ, 604, 420.

This 2-column preprint was prepared with the AAS LaTeX macros v5.2.

Table 1: List of EPs*

Event	Date	Location[a]	Tel[b]	$S_p(R_\odot)$	$Z_{p0}(R_\odot)$	$Z_{p,max}(R_\odot)$	$S_f(R_\odot)$	$Z_{max}(R_\odot)$
1^{+}	1980 Aug 18	SE33	H	0.27	0.12	0.50	0.49	0.66
2^{++}	1988 Aug 16	SE	H	0.17	0.06	0.23	0.31	0.31
3[c]	1999 Sep 14	W90 N37	E, H	0.61	0.11	0.35	1.16	0.60
4	2000 Sep 12	W8 S20	E, H, W	0.48	0.10	0.91	0.90	1.21
5	2001 Apr 23	W62 S33	E, W	0.82	0.17	1.43	1.53	1.91
6^{+++}	2001 Nov 17	E50 S9	R	0.39	0.08	0.50	0.73	0.69
7[d]	2002 Feb 18	E3 S52	R, W	0.43	0.08	1.10	0.82	1.69
7′[d]				0.62	0.08	1.10	1.21	1.72
8	2002 May 22	W50 S14	R, W	0.68	0.14	0.56	1.27	0.85
9	2003 Feb 18	W54 N32	R, W	0.47	0.31	0.36	0.84	0.55
10	2003 Oct 26	W56 S14	R, W	0.39	0.06	0.12	0.75	0.29
11	2004 Feb 15	E90 S32	R, W	0.33	0.13	0.25	0.59	0.38
12	2004 Oct 23	E90 S14	R, W	0.45	0.12	0.43	0.83	0.63
13	2005 Jul 29	E66 N8	H	0.08	0.02	0.05	0.15	0.08

*All heights have been deprojected.

[a]Heliographic coordinates (long, lat) in degrees of the midpoint between two prominence footpoints.

[b]Telescope of observation. W for white-light coronagraph; E for EIT; H for Hα data; R for Nobeyama radio telescope.

[c]Limb event with one footpoint on the front side and the other on the backside of the Sun.

[d]Event on the backside of the Sun. The location is estimated by examining the candidate source region and the rotation of the Sun. The footpoints of the erupting structure were not observed. Entries 7 and 7' correspond to the same event using two different estimates of the footpoint separation distance.

+Prominence at SE limb reportedly extending from S25°–S40° (Vršnak et a. [1993]).

++Prominence reported to be at the SE limb (Vršnak [1990]).

+++Height-time data from Kundu et al. (2004).

Table 2: List of CME events*

Event	Date	Location[a]	$S_f(R_\odot)$	Z_{max}
14^{+}	1997 FEb 23	E75 N35	0.74	0.70
15^{+}	1997 Apr 30	E75 N35	0.47	0.63
16^{b++}	1997 Sep 7	W115 N45	0.71	0.48
17^{c+}	1998 Jun 2	W90 S60	1.60	1.20

*All heights have been deprojected.

[a]Heliographic coordinates (long, lat) of the midpoint between two footpoints.

[b]Event on the backside of the Sun. The location is estimated by examining the candidate source region and the rotation of the Sun. Z_0 is determined from EIT images as the candidate source region rotated around the west limb.

[c]Limb event with one footpoint on the front side and the other on the backside of the Sun.

+From Chen and Krall (2003).

++From Chen et al. (2001).

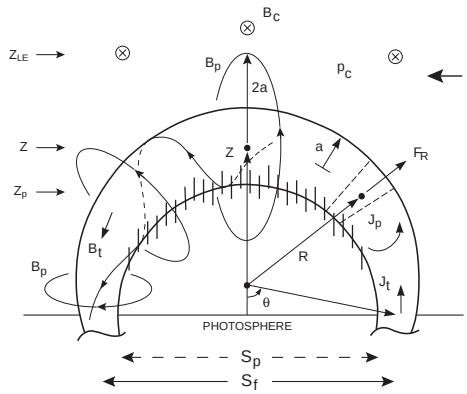

Fig. 1.— Schematic of a flux rope above the photosphere. The toroidal loop structure is the current channel with major radius R and minor radius a. The toroidal J_t and poloidal J_p currents and the corresponding poloidal B_p and toroidal B_t magnetic field components are indicated. Coronal pressure p_c and the overlying coronal field B_c (in the toroidal direction) are indicated. The outermost flux surface, represented by three poloidal field lines, is at $r = 2a(\theta)$ from the toroidal axis of the current channel, where $a(\theta)$ is the local minor radius at angular position θ. The centroid of the apex of the flux rope is at height Z from the base of the corona. The CME leading edge (LE) is at height $Z_{LE} = Z+2a_a$ at the apex. The apex of the prominence is at $Z_p = Z - a_a$. These heights are indicated by the arrows on the left. The flux-rope footpoints are separated by S_f, measured center to center. The prominence footpoints are separated by $S_p = S_f - 2a_f$. Adapted from Figures 1 and 2 of Chen (1996), combining the information in the two figures, including the prominence in the flux-rope structure.

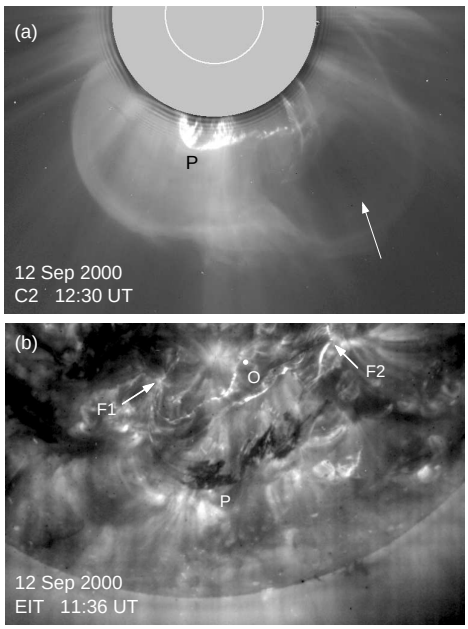

Fig. 2.— A CME-EP event that illustrates the geometry given in Figure 1. (a) A LASCO/C2 white-light image taken at 1230 UT on 2000 September 12. A relatively dark cavity is evident to the right, corresponding to a slightly oblique projection of a minor cross-section. The apex of the LE is taken to be at Z_{LE} (Figure 1). An associated eruptive prominence (EP), designated by P, is at height Z_p. (b) A view of the source region of eruption, observed by EIT (195 Å) at 1136 UT. The EP appears as a dark feature in absorption. The footpoints $F1$ and $F2$ are indicated. Point O marks the midpoint between $F1$ and $F2$. The heliographic coordinates of O are used to deproject height measurements.

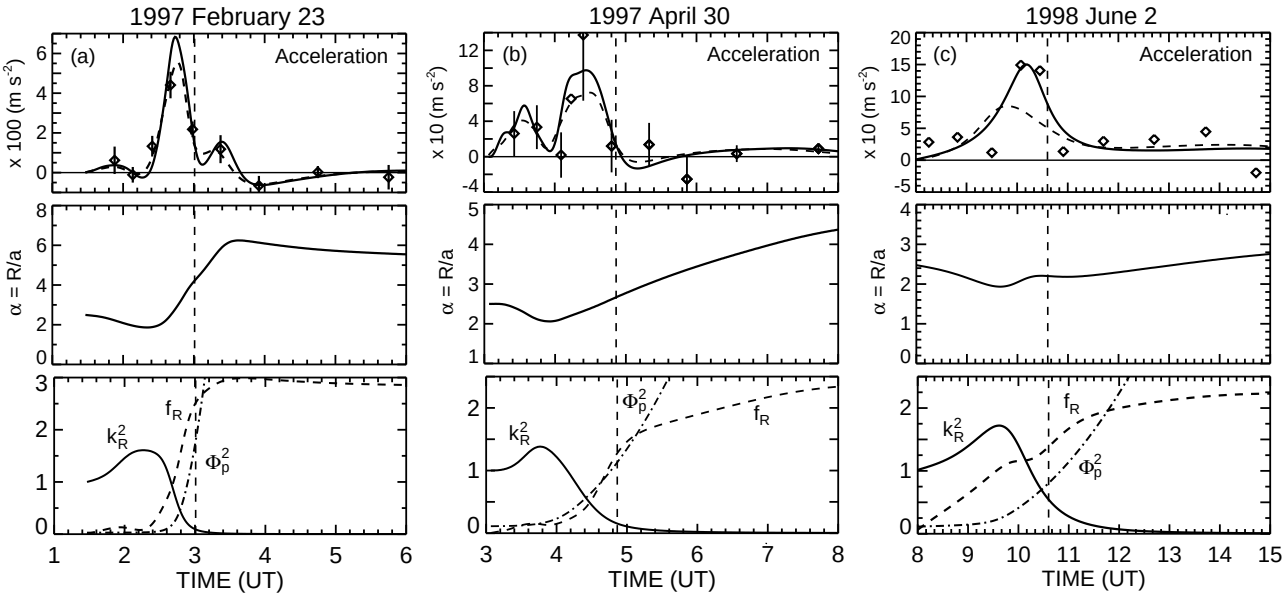

Fig. 3.— Top panels: Acceleration of the CME LE (diamonds). Theoretical solutions for the acceleration of LE (solid curves) and centroid of the apex (dashed curves) are shown. For each event, the main acceleration phase is to the left of the vertical dashed line. The residual acceleration phase is to the right. Middle panels: Ratio $\alpha = R/a$ versus time of the model flux ropes shown in relation to the acceleration profiles. Bottom panels: $k_R^2(t)$, $\Phi_p^2(t)$, and $f_R(t)$ are shown in relation to the acceleration profiles. The acceleration curves are the products of these functions.

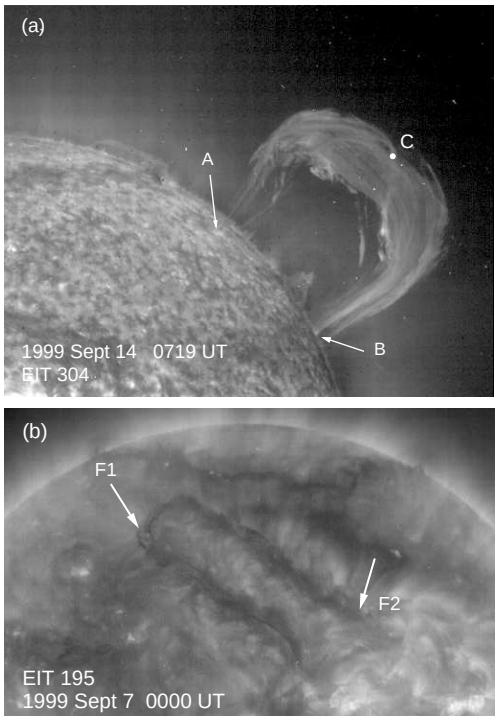

Fig. 4.— (a) EIT (304 Å) image at 0719 UT on 1999 September 14 (event 3), showing an eruptive prominence with clearly visible legs, which are indicated by A and B. (b)EIT (195 Å) image of the presumed source region taken approximately one week earlier, showing a U-shaped filament channel. $F1$ and $F2$ are identified with points A and B, respectively. The magnetograms from the Michelson Doppler Imager (MDI) on board SOHO indicate the presence of a U-shaped neutral line corresponding to the filament channel.

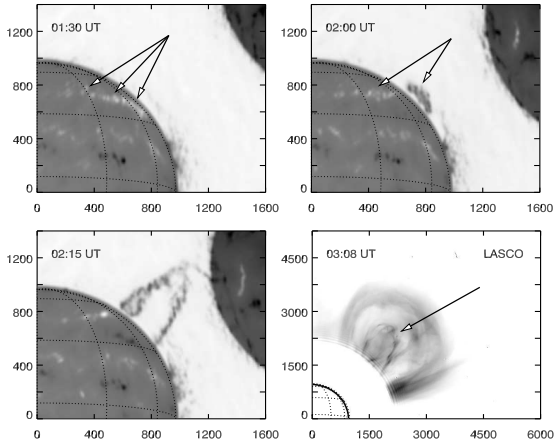

Fig. 5.— Nobeyama Radioheliograph images and LASCO C2 (fourth panel) image of the eruption on 2003 February 18 (event 9). This event was also observed by the Mauna Loa Solar Observatory. The axes are in units of arc seconds.

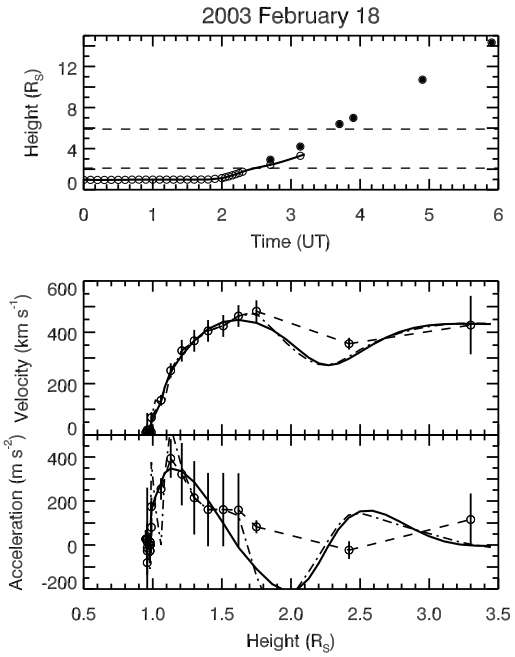

Fig. 6.— Analysis of event 9. From the top: heliocentric height-time, velocity-height, and acceleration-height data. The horizontal dashed lines in the top panel bound the C2 field of view. In the bottom two panels, the solid curves show the filtered data. The dashed curves connect the raw data, and the dash-dot curves are the re-interpolated data. Z_{max} is determined as the height of maximum acceleration at the prominence apex. Z_{max} can be estimated from the width of the peak acceleration-height profile. This uncertainty increases with S_f.

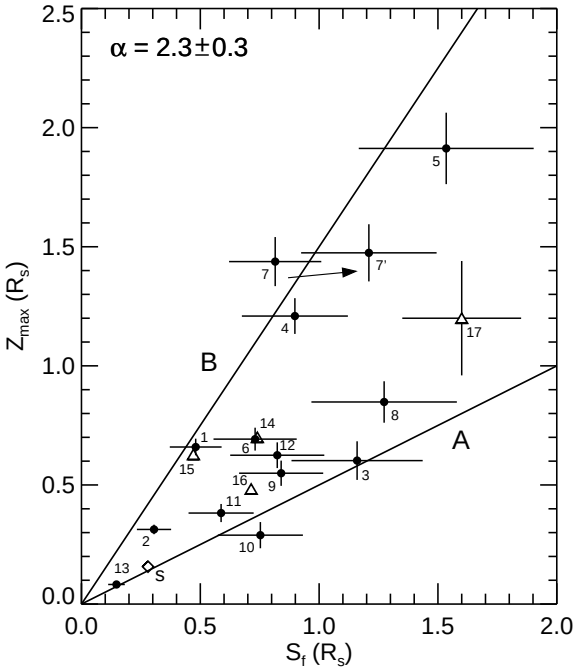

Fig. 7.— Plot of observationally determined S_f versus Z_{max}. EPs are represented by solid circles, and CMEs are shown as open triangles. The uncertainty in α, taken to be $\Delta\alpha = \pm 0.3$, results in uncertainties in both S_f and Z_{max}. The error bars show the estimated total error due to height measurements and $\Delta\alpha$. Data points 7 and 7' correspond to the smaller and larger of the two possible values of S_p, respectively, for the backside event 7. Diamond marked s is an MHD simulation.

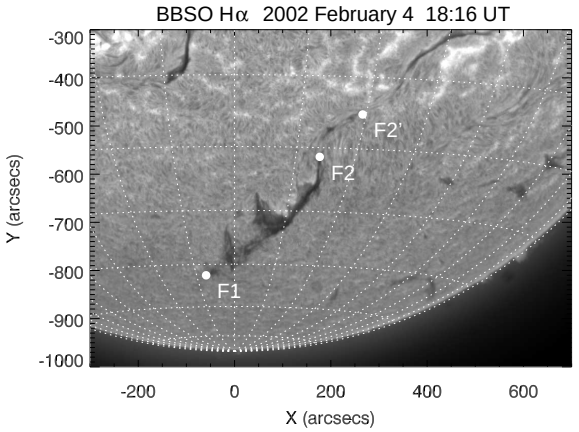

Fig. 8.— Hα image of the candidate source region for the 2002 February 18 event. Using $F1$ and $F2$ as the footpoints gives data point 7 in Figure 7. Using $F1$ and $F2'$ yields data point 7'.